

The Infrared Camera (IRC) deep survey in the performance verification phase

Takehiko WADA,¹ * Shinki OYABU,¹ Yoshifusa ITA,¹ Hideo MATSUHARA,¹ Chris P. PEARSON,^{1,2} Takashi ONAKA,³ Youichi OHYAMA,¹ Fumihiko USUI,¹ Naofumi FUJISHIRO,¹ Daisuke ISHIHARA,³ Hirokazu KATAZA,¹ Woojung KIM,¹ Toshio MATSUMOTO,¹ Hiroshi MURAKAMI,¹ Itsuki SAKON,³ Toshihiko TANABÉ,⁴ Toshinobu TAKAGI,¹ Kazunori UEMIZU,¹ Munetaka UENO,⁵ and Hidenori WATARAI⁶

¹*Institute of Space and Astronautical Science, Japan Aerospace Exploration Agency, Sagami-hara, Kanagawa 229 8510*

²*ISO Data Centre, ESA, Villafranca del Castillo, Madrid, Spain.*

³*Department of Astronomy, School of Science, University of Tokyo, Bunkyo-ku, Tokyo 113-0033*

⁴*Institute of Astronomy, University of Tokyo, Mitaka, Tokyo 181-0015*

⁵*Department of Earth Science and Astronomy, Graduate School of Arts and Sciences, The University of Tokyo, Meguro-ku, Tokyo 153-8902*

⁶*Office of Space Applications, Japan Aerospace Exploration Agency, Tsukuba, Ibaraki 305-8505*

(Received 2007 June 3; accepted 2007 August 14)

Abstract

We report the first results of a near- and mid- infrared deep survey with the Infrared Camera (IRC) onboard AKARI in the performance verification phase. Simultaneous observations by the NIR, MIR-S and MIR-L channels of the IRC with effective integration times of 4529, 4908, and 4417 seconds at 3, 7, and 15 μm , covering 86.0, 70.3, and 77.3 arcmin² area, detected 955, 298 and 277 sources, respectively. The 5 σ detection limits of the survey are 6.0, 31.5 and 71.2 μJy and the 50 % completeness limit are 24.0, 47.5, and 88.1 μJy at 3, 7, and 15 μm , respectively. The observation is limited by source confusion at 3 μm . We have confirmed the turnover in the 15 μm differential source counts around 400 μJy , previously detected by surveys with the Infrared Space Observatory. The faint end of 15 μm raw source counts agree with the results from the deep surveys in the GOODS fields carried out with the *Spitzer* IRS peak up imager and the predictions of current galaxy evolution models. These results indicate that deep surveys with comprehensive wavelength coverage at mid-infrared wavelength are very important to investigate the evolution of infrared galaxies at high redshifts.

Key words: space vehicles: instruments — galaxies: statistics — infrared: galaxies

1. Introduction

The Infrared Camera (IRC; Onaka et al. 2007; Wada et al. 2002) is a near- and mid- infrared scientific instrument onboard the first dedicated Japanese infrared astronomical satellite AKARI (Murakami 2007). The unique instrumental features of the IRC, compared to the similar contemporary IRAC instrument on the *Spitzer* Space Telescope (Fazio et al. 2004), are a wider field of view (FOV; 10×10 arcmin²) and a more comprehensive contiguous wavelength coverage (2-26 μm) with a larger numbers of filters (9 bands) of comparable sensitivity to IRAC. A deep and wide field near- and mid- infrared survey (LS NEP DEEP) covering these wavelengths by all the 9 bands is underway in the North Ecliptic Pole (NEP) region (Matsuhara et al. 2006).

Previous deep surveys at mid-infrared wavelengths have made the striking discovery of a bump in the Euclidean-normalized differential source counts around 0.4 mJy at 15 μm in the ISO/ISOCAM surveys (Elbaz et al. 1999) and 0.3 mJy at 24 μm in the *Spitzer* MIPS surveys (Papovich

et al. 2004). Marleau et al. (2004) compared the 15 μm and 24 μm source counts adopting a 24/15 μm flux ratio of 1.2, which was derived from the SED template of Chary & Elbaz (2001). They found that a shift in the turnover of the Euclidean-normalized counts, however, the fainter side of 15 μm counts was not well constrained due to the limitation of the sensitivity and areal coverage of the ISO surveys. Pearson (2005) showed that models incorporating either a burst of evolution or a more smoother continuous evolution could simultaneously reproduce both the 15 μm ISO and 24 μm *Spitzer* counts and concluded that revealing the dominant population at the fainter end of the 15 μm counts (e.g., starburst, LIRGs, ULIRGs) was an important point to be resolved.

One of the objectives of the LS NEP DEEP survey is to reveal the nature of the faint 15 μm population through a deep and wide multi-band survey together with the SED fitting technique focused on the PAH emission and the silicate absorption features (Takagi & Pearson 2005). Note that although *Spitzer* also has the capability, via its IRS 16 μm peak-up Imaging (PUI) mode, for imaging in this wavelength range (Teplitz et al. 2005a; Kasliwal et al. 2005), however, the FOV of the 16 μm PUI mode is very small ($1' \times 1'$; 100 times smaller compared to that

* Further information contact Takehiko Wada (wada@ir.isas.jaxa.jp)

of the IRC), and moreover, there still exists a gap in the wavelength coverage between the IRS $16\mu\text{m}$ PUI and the shorter $8\mu\text{m}$ IRAC band.

In order to evaluate the capability of such a deep and wide survey by the IRC, we have conducted a pilot survey in both the imaging and spectroscopic modes with 10 pointed observations for each mode at the end of the performance verification phase of the AKARI satellite.

In this paper, we report on the first results of the pilot imaging survey. The result of the corresponding pilot spectroscopy survey will be reported elsewhere. In this work, section 2 describes the observations. In section 3, the data reduction is presented, source extraction and photometry are described in section 4, section 5 describes the estimation of sensitivity and completeness of the survey. Finally, we discuss the capability of the IRC in deep survey mode and the $15\mu\text{m}$ source counts in section 6.

2. Observation

2.1. AOT for deep surveys

Since the main objective of the AKARI mission is the far-infrared All-Sky Survey (Pearson et al. 2007), the orbit is by design a Sun-synchronous polar orbit which puts severe constraints on the visibility of individual target fields on the sky. Thus, the operation for any pointed observations have been made as simple as possible, producing strong constraints on the Astronomical Observation Templates (AOT) for the IRC pointed observations such as (1) fixed frame integration time, (2) no mapping mode in a single pointed observation (approximately 10 minutes), that were not apparent for infrared space observatories such as *Spitzer* or the Infrared Space Observatory (ISO)¹.

A series of three AOT sets for pointed observations with the IRC have been prepared. The first set, referred to as IRC02 and IRC03, are for medium deep multi-band surveys, in which both changes of filters and dithering in target position is performed. The second set are for deep surveys and are referred to as IRC00 and IRC05, in which no filter change and no dithering is performed, in order to minimize the dead time and maximize the observation time. For the IRC00 and IRC05 AOTs, at least three pointed observations are required in order to ensure redundant and reliable observations. The third AOT set, referred to as IRC04 is designed for spectroscopic observations and is described elsewhere (Ohyama et al. 2007).

Using the AOTs designed for deep surveys, a deep and wide field near- and mid- infrared survey (LS NEP DEEP) is underway in the North Ecliptic Pole (NEP) region (Matsuhara et al. 2006). In order to evaluate the capability of deep imaging surveys by the IRC, we have conducted a pilot survey with 10 pointed observations.

¹ These constraints make the IRC inefficient for wide shallow surveys in which a depth of one pointed observation or better is not required. We have prepared a separate IRC scanning mode for such a shallow and wide surveys including the IRC All-Sky Survey at mid-infrared wavelengths (Ishihara et al. 2006).

2.2. pilot survey

The observations were executed from April 29 to May 6 in 2006, almost at the end of the performance verification (PV) phase of AKARI. We selected a target position of $(\alpha, \delta)=(268.88, 66.61)$, chosen by the following reasons. (1) The FOV of the NIR and MIR-S channels must be within the continuous viewing zone of AKARI (CVZ: within 0.6 degree from the North or South ecliptic poles). (2) The field must be well studied by the other observations in order to make cross-identification of the AKARI sources. The deep multi-color optical images (Wada et al. 2007) taken by Subaru/Suprime-Cam (Miyazaki et al. 2002) were used for this purpose. (3) The field must have few bright objects in order to make the deep survey. We carefully selected a field, which had no bright stars, in the Suprime-Cam image field.

We used the AOT for deep observation (IRC00) with an AOT filter combination parameter of “b”, which corresponds to the filter set of the N3 ($3.3\mu\text{m}$), S7 ($7.0\mu\text{m}$) and L15 ($15.0\mu\text{m}$) band filters, for the NIR, MIR-S and MIR-L channels, respectively. We used a target position parameter of “N”, which means that the center of the FOV of the NIR channel (and simultaneously, the MIR-S channel which observes the same point on the sky via a beam splitter) targeted the specified coordinates, while that of the MIR-L channel was pointed at a parallel field, around 25 arcmin apart from that of the NIR/MIR-S. No dithering operation between pointed observations were made, i.e. we used the same target position for all pointed observations². However, the FOV of the NIR/MIR-S rotates around the center of the field as the direction of the Sun changes (approximately one degree per day), resulting in good redundancy except at the very center of the FOV. Note that good redundancy in the observations is possible over the entire FOV of the MIR-L channel, since the FOV of the MIR-L rotates around the FOV of NIR/MIR-S. Details of the observation parameters are summarized in Table 1.

Typically, 10 and 30 frames with effective exposure times of 44.4 and 16.4 seconds in each frame were obtained for a single pointed observation, for the NIR and MIR-S/L channels, respectively. The total exposure time was 4530, and 4908 and 4417 seconds, for the NIR, MIR-S and MIR-L channels, respectively.

3. Data reduction

The data were reduced by the standard IRC imaging pipeline (version 060801; see IRC Data User Manual, Lorente et al. 2007). The dark frame (version 060428), which was measured just before the PV phase observations began, was subtracted. Flat fielding was performed based on the flat field frame (version 060626), which was created from 6 pointed observations of a high background region near the ecliptic plane with the AOT IRC02. Distortion correction (version 060529) was performed based on the

² Dithering operation between pointed observations have already implemented in the observations after 2006-09-24T09:00:00

Table 1. Observation log

Target id	AOT	OBS-DATE	N/S position		L position	
			RA	DEC	RA	DEC
5020053.1	IRC00 b;N	2006-05-03T03:32:41	268.88	66.61	269.31	66.90
5020053.2	IRC00 b;N	2006-05-03T06:50:31	268.88	66.61	269.31	66.90
5020053.3	IRC00 b;N	2006-05-03T20:02:41	268.88	66.61	269.30	66.90
5020053.4	IRC00 b;N	2006-05-03T21:41:17	268.88	66.61	269.30	66.90
5020053.5	IRC00 b;N	2006-05-03T23:21:02	268.88	66.61	269.30	66.90
5020054.1	IRC00 b;N	2006-04-29T20:18:56	268.88	66.61	269.35	66.89
5020054.2	IRC00 b;N	2006-04-30T07:52:33	268.88	66.61	269.34	66.89
5020054.3	IRC00 b;N	2006-04-30T09:31:47	268.88	66.61	269.34	66.89
5020055.1	IRC00 b;N	2006-05-06T00:52:01	268.88	66.61	269.28	66.91
5020055.2*	IRC00 b;N	2006-05-06T05:49:13	268.88	66.61	269.27	66.91

* MIR-L Data in this observation were not used.

Table 2. Summary of the survey

band	area (arcmin ²)	N_F^*	T_{integ}^\dagger (sec)	N_S^\ddagger	5σ limit [§] (μ Jy)	50% limit (μ Jy)
N3	86.0	102	4529	955	6.0	24.0
S7	70.3	300	4908	298	31.5	47.5
L15	77.3	270	4417	277	71.2	88.1

* Number of frames co-added.

† Total integration time.

‡ Number of source detected.

§ Detection limit (sky noise limit).

|| Completeness limit.

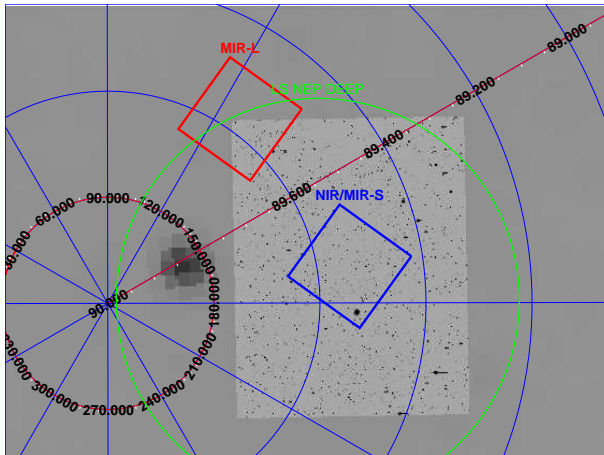


Fig. 1. The locations of the survey fields and the SUBARU/Suprime-Cam deep z' band image, superposed on IRAS 12 micron map. Blue box and red box are 10×10 arcmin field of view of the NIR/MIR-S and MIR-L channels, respectively. The N3 and S7 fields are covered by the Suprime-Cam image, while the L15 field is partially covered by the Suprime-Cam image. The axes shown in the figure are in ecliptic coordinate. The field of the AKARI large area deep survey (LS NEP DEEP) is indicated as a green circle.

data obtained from the observations of globular clusters in the PV phase (Ita et al. 2007). After the reduction of individual frames, we co-added all the frames together.

In co-adding, we subtracted the self sky image from each individual frame which was created by median filtering with 20×20 pixel kernel, in order to remove the effect of stray light from the Earth shine. Alignment of the frames was determined by the position of the point sources in each frame in the case of the NIR and MIR-S channels. In case of the MIR-L channel, the number of the point sources which had sufficient signal-to-noise ratio was not sufficient. Therefore, in order to align the MIR-L frames, we used the alignment of the MIR-S frames, which were simultaneously observed with the MIR-L in a parallel field, using the “coaddLusingS”, an optional task in the IRC pipeline. All the 10 pointing data were co-added at once by the pipeline in case of the NIR and MIR-S channel. The task “coaddLusingS” which was used for the MIR-L data does not support a rotation of the FOV and currently cannot handle multi-pointing data. Therefore, we co-added the MIR-L frames in each pointed observation in order to improve the signal-to-noise ratio, and then co-added the frames referring to positions of the point sources detected in each frame.

Any spurious events, such as cosmic ray events, moving debris, optical and electronic ghost images were removed at the co-addition stage using a 3 sigma clipping

technique. We used the “ccdclip” option (in which the detector noise performance were assumed) rather than the default option “sigclip” (in which the noise performance is estimated from the data itself). The average value among the frames, instead of the median value, for each pixel was computed in order to improve the signal-to-noise ratio of the final image.

The number of frames which were successfully co-added were 102, 300 and 270 in the N3, S7 and L15 bands, respectively (the L15 band data taken with the target ID=5020055.2 was not used since the pipeline failed to co-add the L15 data, probably because of large stray light from the Earth shine). One IRC pointing consists of long exposure frames together with short exposure frames to obtain a wider dynamic range. However, we co-added the long exposure frames only.

Astrometry was based on a comparison of the positions of the point sources detected in the AKARI image and sources listed in the 2MASS point source catalog. For the N3 and S7 band images, a build-in function of the pipeline successfully identified the AKARI sources with the sources in 2MASS catalog. For the L15 band image, automatic matching failed due to the intrinsic red K - L15 color of the L15 sources. We identified the 2MASS sources by eye for the L15 band images. Cross identification with the Subaru/Suprime-Cam deep optical image showed that the positional accuracy was better than 2 pixel.

Finally, we trimmed the area close to the edge of each co-added image in which the signal-to-noise ratio was poor. The area of the final images are 85.95, 70.27 and 77.29 arcmin², for the N3, S7, and L15 bands, respectively. Figures 2, 3 and 4 show the final images in the N3, S7, and L15 bands, respectively.

4. Source extraction and photometry

SExtractor (Bertin & Arnouts 1996) was used for source extraction. The extraction criterion was a connection of five pixels having more than a 1.6532 sigma significance above local sky fluctuation. If the flux is equally distributed over these five pixels, it corresponds to a 5 sigma detection. The actual PSF has a weak concentration at its center, and the above criterion gives a slightly higher significance than a 5 sigma detection for a point source.

The flux of each extracted source was evaluated by aperture photometry calculated in SExtractor. Elliptical aperture photometry with variable size (SExtractor’s MAGAUTO) was used for the further analysis. Parameters of “Kron factor” and “minimum radius” were set to the default values of 2.5 and 3.5, respectively. The actual apertures used for each detected source are overlaid on the AKARI/IRC images in the figures 5, 6 and 7. Magnitude zero point was derived by observations of standard stars, and is described in Lorente et al. (2007).

Simple aperture photometry (SExtractor’s MAGAPER) was also calculated in order to estimate the amount of aperture correction. The aperture radius was set to the same as used in the standard star observations, 10 and

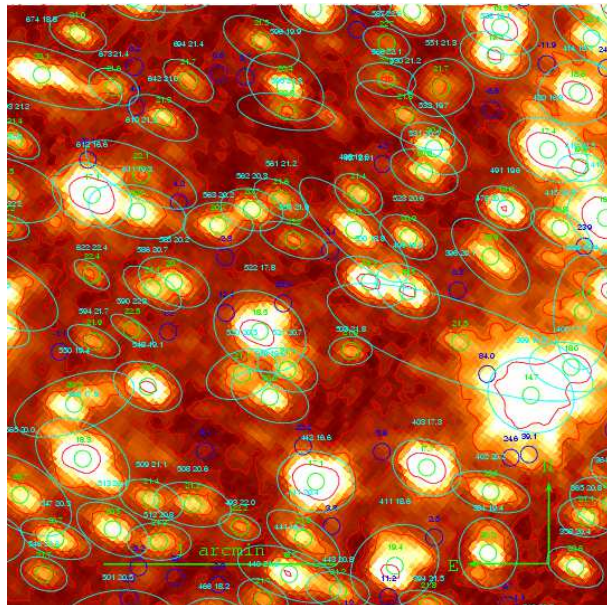


Fig. 5. Close up view of the AKARI/IRC N3 band image. Contours are 1, 3 and 10 sigma levels of the local background fluctuation. The green circles indicate the positions of detected sources. The MAGAUTO apertures (cyan) are superposed on each AKARI source. The blue circles indicate the apertures on blank sky positions which were used for the calculation of the detection limit.

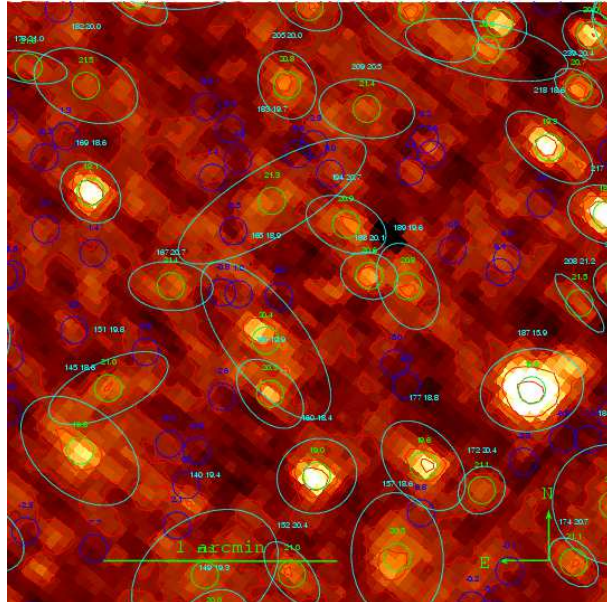


Fig. 6. Close up view of the AKARI/IRC S7 band image. Contours are 1, 3 and 10 sigma levels of the local background fluctuation. The green circles indicate the positions of detected sources. The MAGAUTO apertures (cyan) are superposed on each AKARI source. The blue circles indicate the apertures on blank sky positions which were used for the calculation of the detection limit. Some of peaks which have not detected as a source by our simple detection criterion have counter parts in the deep optical image. Further optimization of detection criterion may improve the detection limit.

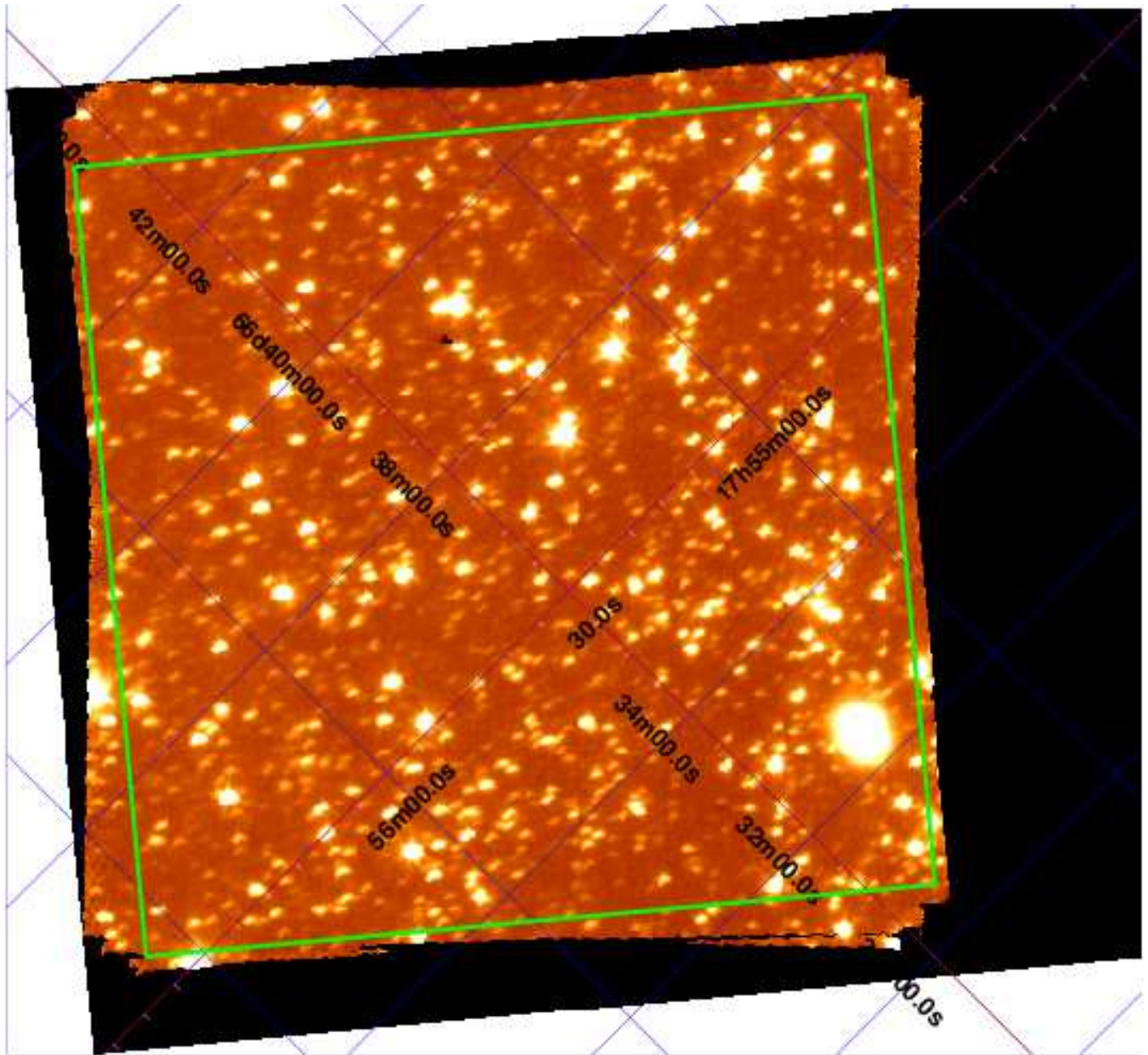


Fig. 2. The final N3 co-added image is shown in equatorial coordinates (rotated 45 degrees counter-clockwise). The green box indicates the region over which point source extraction was performed. The size of region is 9.19 x 9.19 arcmin.

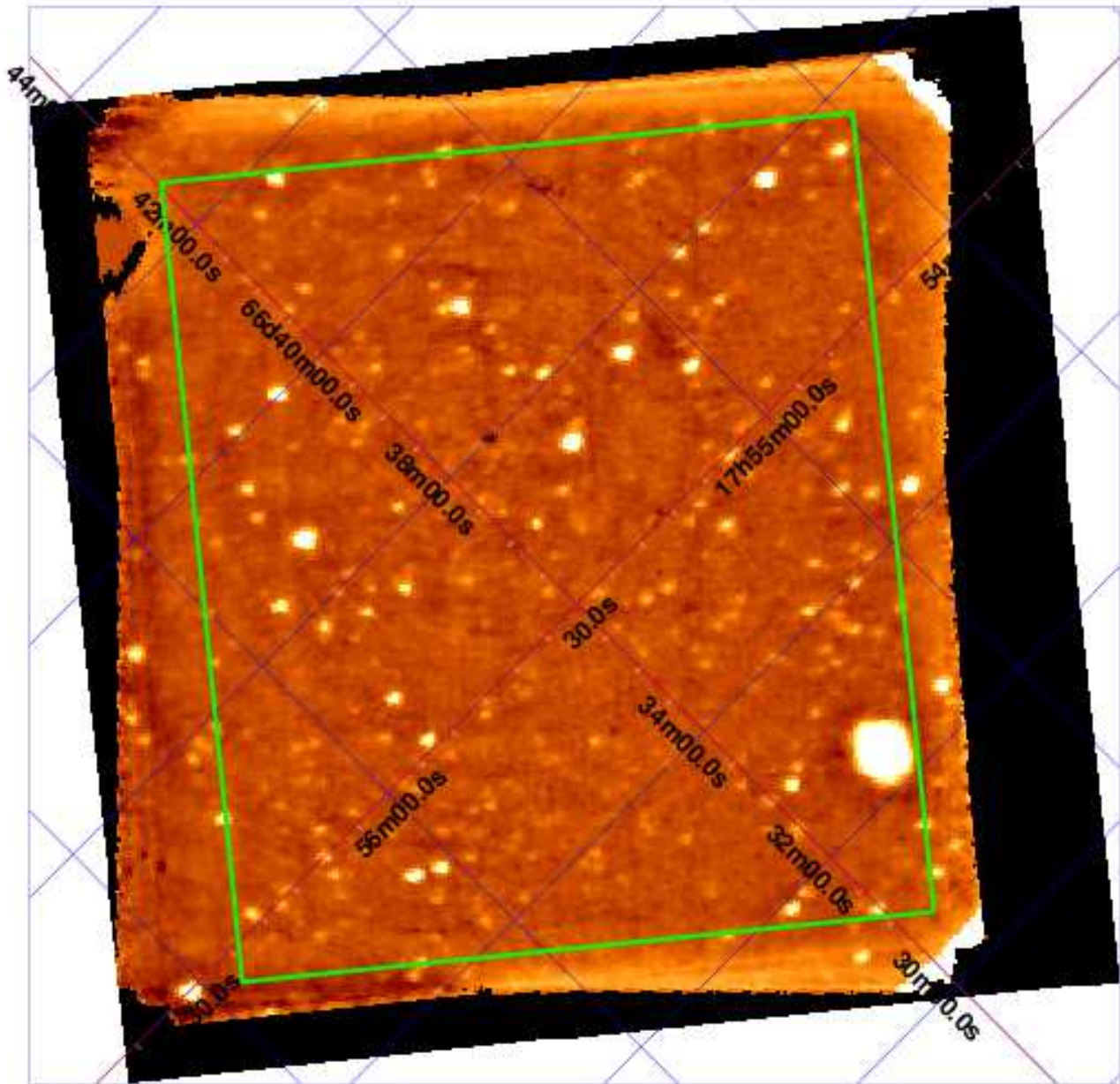


Fig. 3. The final S7 co-added image is shown in equatorial coordinates (rotated 45 degrees counter-clockwise). The green box indicates the region over which point source extraction was performed. The size of region is 7.76 x 8.96 arcmin.

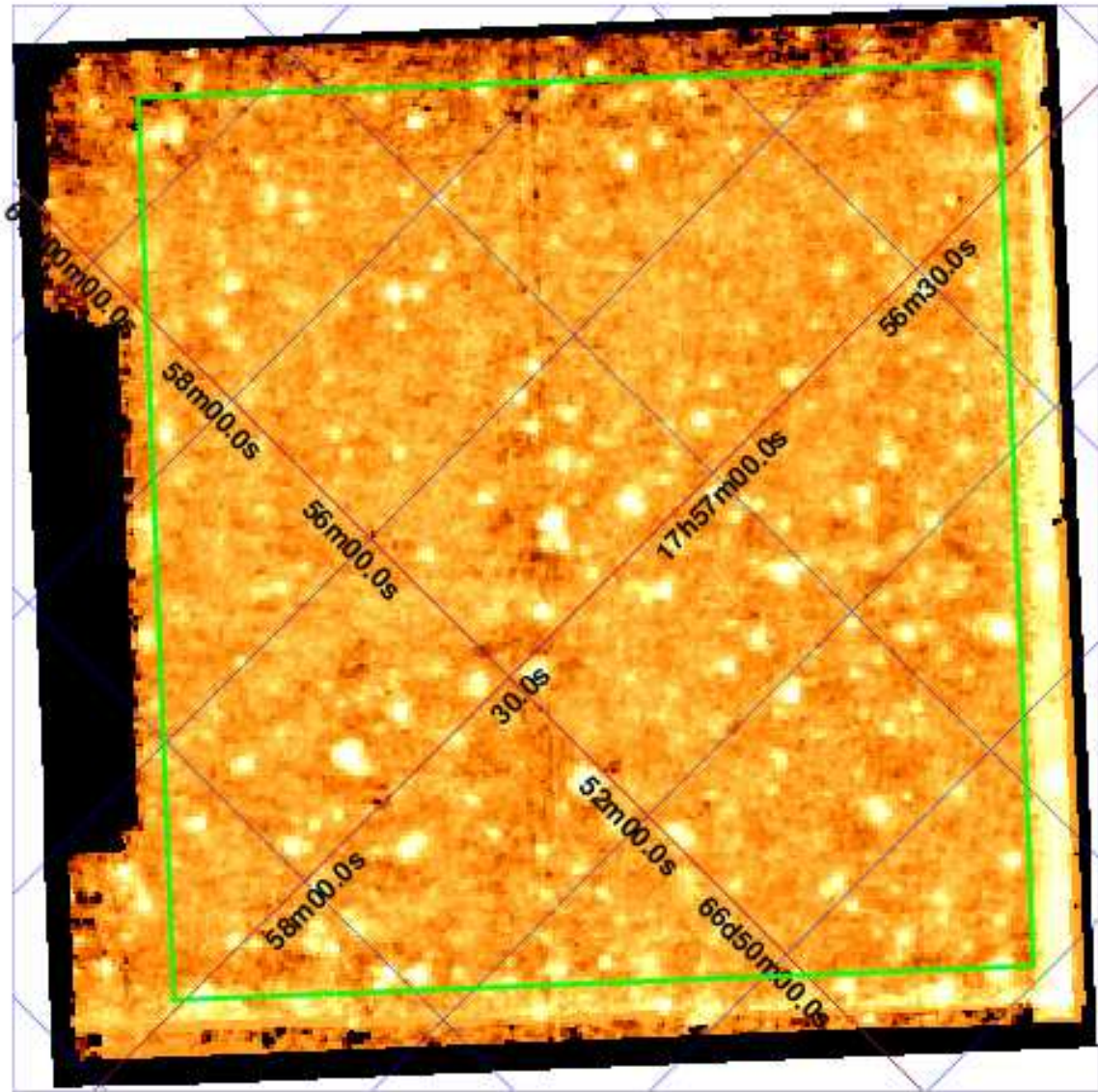


Fig. 4. The final L15 co-added image is shown in equatorial coordinates (rotated 45 degrees counter-clockwise). The green box indicates the region over which point source extraction was performed. The size of region is 8.77 x 9.21 arcmin.

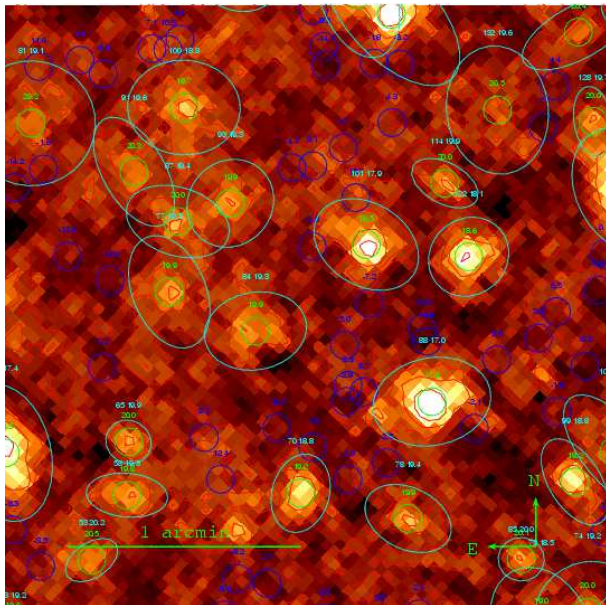


Fig. 7. Close up view of the AKARI/IRC L15 band image. Contours are 1, 3 and 10 sigma levels of the local background fluctuation. The green circles indicate the positions of detected sources. The MAGAUTO apertures (cyan) are superposed on each AKARI source. The blue circles indicate the apertures on blank sky positions which were used for the calculation of the detection limit.

7.5 pixels in the NIR and MIR-S/L images, respectively. Figure 8 shows the comparison between the flux estimations by MAGAUTO and MAGAPER for each source. We did not apply any aperture correction for further analysis because the results using MAGAUTO and MAGAPER were reasonably consistent.

5. Estimation of sensitivity and completeness

5.1. detection limit (sky noise limit)

The sensitivity of the point source extraction was estimated by measuring the fluctuation of the photometry on blank sky at random position (sky noise). The positions which were close to a source were not used for the measurement in order to avoid source contamination effects.

We made simple aperture photometry (a no weighting, no PSF fitting technique was applied, and no centering was performed) at each random position using the IRAF/PHOT package. The size of aperture radius was set to 1.5 pixel for all three bands. The aperture had slightly wider area (7.0 pixels) than the minimum number of connected pixels in the extraction criterion (5 pixels), a slightly worse estimation of the sensitivity resulted from this choice of aperture size. The actual apertures which were used for above measurement are shown in the figures 5, 6 and 7.

In order to evaluate the fluctuation of photometry, the histogram of the photometry was fit with a Gaussian function. We define the one sigma level of the fluctuation as the standard deviation of the Gaussian. Finally, tak-

ing into account the aperture correction, we calculate a 5 sigma detection limit for a point source.

The 5 sigma detection limits are estimated to be 11.2, 71.3 and 201 μJy for the co-added images obtained in a single pointed observation, and 6.0, 31.5 and 71.2 μJy for that in the ten pointed observations, in the N3, S7, L15 bands, respectively. The results of the detection limit estimation are summarized in Table 4.

The improvements from one to ten pointings were a factor of 1.87, 2.27 and 2.82 in the N3, S7, and L15 bands, respectively. These factors in the N3 and S7 bands are slightly worse than what is expected from the increase of number of observations (i.e., square root of ten).

5.2. completeness correction

The completeness of the source extraction was estimated via Monte Carlo simulations. We added artificial sources from a truth catalog into the final co-added images, and then extracted the sources again using the same extraction parameters. We, then, compared the position and magnitude of input sources with the extracted sources. If there was a extracted source within 2 pixels around an input source and if the difference in magnitude between the input source and the extracted source was less than 0.5 magnitude, we regarded the event as a successful extraction of an artificial truth source, and counted it.

We define the completeness of the source extraction as the number of successfully extracted truth sources divided by the total number of artificial input sources that were originally added into the original image.

The calculation was performed by dividing our flux range into magnitude bins of size 0.2 magnitudes (i.e. uniform bin size in log Jy) and populating each bin with 20 artificial sources. The magnitude distribution of the sources was normalized to a flat Euclidian universe in each bin. These 20 sources were then added in random positions in the image, assuming a circular PSF. In order to avoid self-confusion effects among the artificial sources, we did not insert a source if the minimum distance to another artificial source was less than 20 pixels. Note that the number of random sources that can be input at any one time is constrained by the array size of the IRC (NIR: 412×512 pixels, MIR-S/L: 256×256 pixels).

In order to improve the statistical significance of the Monte Carlo simulations, we performed 20 statistically independent calculations for each magnitude bin, creating an effective total of 400 artificial sources. The simulation was then subsequently carried out for each magnitude bin in turn.

In order to estimate the error in the calculation of the completeness, we then performed 25 statistically independent sets of the above simulations. The results are shown in the figure 9, and the completeness limits are summarized in table 4.

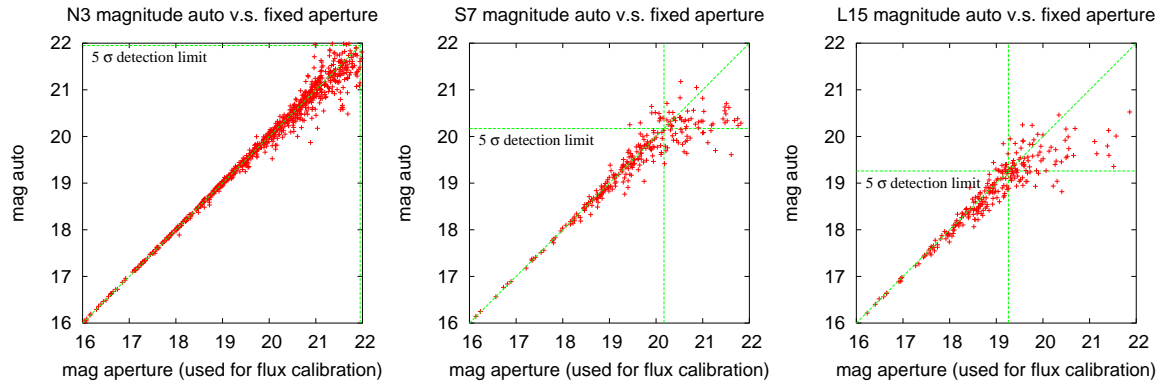


Fig. 8. Magnitudes of individual stars given by MAGAUTO are compared with that by MAGAPER with the same aperture radius as the observations of the standard stars. No significant systematic difference between MAGAUTO and MAGAPER is seen above the 5σ detection limit, although there is large systematic difference at fainter level.

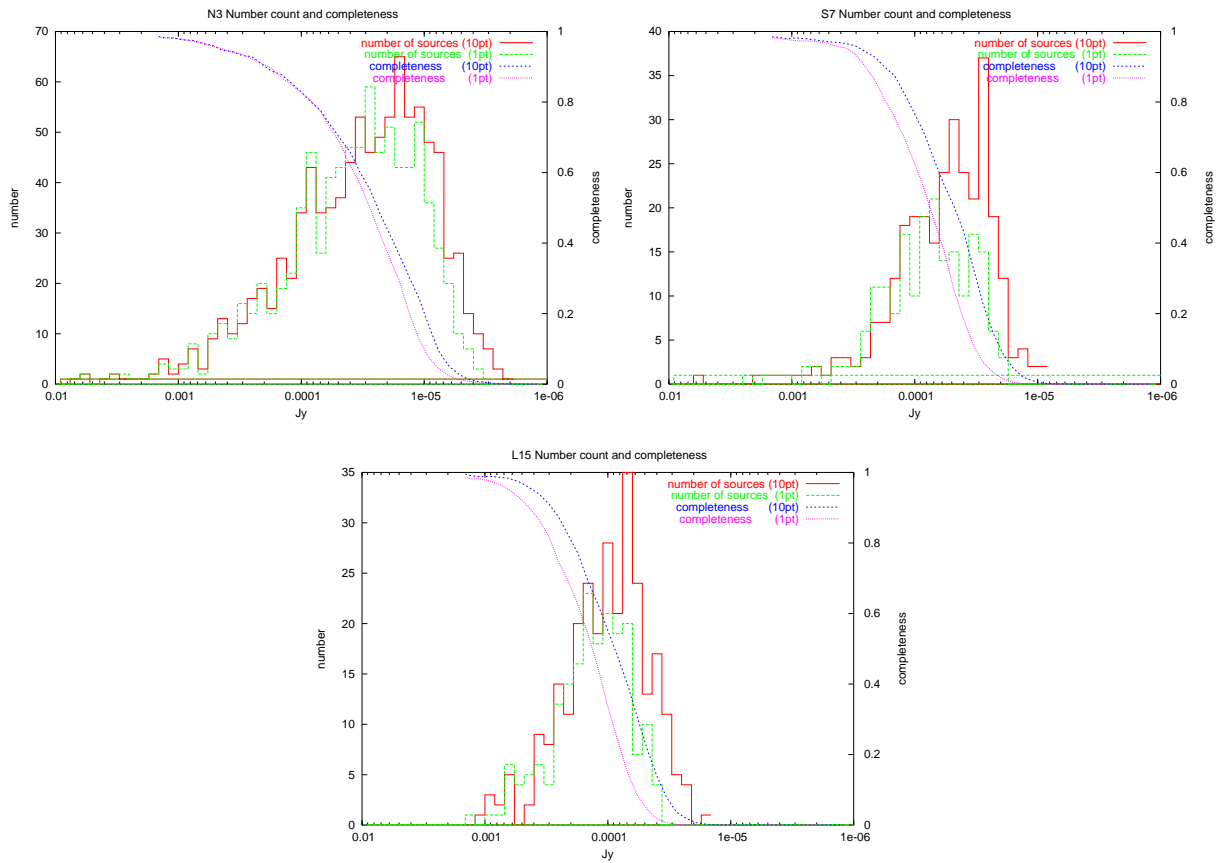


Fig. 9. Differential source counts and completeness estimation is shown for the N3, S7, and L15 bands, respectively. The results from both a single pointed and ten pointed observations are plotted.

Table 3. Source counts and completeness

mag _{AB}	log(Jy)	N3			S7			L15		
		N*	\bar{C}^\dagger	$\sigma(C)^\ddagger$	N	\bar{C}	$\sigma(C)$	N	\bar{C}	$\sigma(C)$
<15.8	> -2.76	10			3			0		
15.8–16.0	-2.80	2	0.986	0.007	1	0.985	0.006	0	0.995	0.002
16.0–16.2	-2.88	5	0.983	0.005	1	0.984	0.006	0	0.992	0.005
16.2–16.4	-2.96	2	0.981	0.005	1	0.980	0.005	1	0.988	0.005
16.4–16.6	-3.04	4	0.976	0.006	1	0.982	0.005	3	0.989	0.006
16.6–16.8	-3.12	7	0.975	0.008	1	0.979	0.008	2	0.987	0.006
16.8–17.0	-3.20	3	0.966	0.009	2	0.975	0.007	5	0.983	0.005
17.0–17.2	-3.28	9	0.961	0.009	1	0.972	0.009	0	0.973	0.005
17.2–17.4	-3.36	13	0.946	0.009	3	0.969	0.007	2	0.958	0.006
17.4–17.6	-3.44	10	0.943	0.010	3	0.966	0.008	9	0.940	0.009
17.6–17.8	-3.52	12	0.932	0.010	2	0.959	0.009	8	0.911	0.014
17.8–18.0	-3.60	17	0.929	0.010	3	0.943	0.011	14	0.874	0.018
18.0–18.2	-3.68	19	0.907	0.015	7	0.927	0.012	11	0.822	0.020
18.2–18.4	-3.76	15	0.888	0.015	7	0.898	0.015	20	0.770	0.023
18.4–18.6	-3.84	25	0.878	0.016	12	0.874	0.016	24	0.692	0.016
18.6–18.8	-3.92	21	0.854	0.019	18	0.822	0.013	19	0.627	0.022
18.8–19.0	-4.00	34	0.829	0.019	19	0.767	0.022	28	0.554	0.023
19.0–19.2	-4.08	43	0.801	0.021	19	0.711	0.023	21	0.480	0.026
19.2–19.4	-4.16	34	0.775	0.021	16	0.635	0.026	35	0.401	0.016
19.4–19.6	-4.24	35	0.734	0.024	24	0.566	0.028	24	0.307	0.025
19.6–19.8	-4.32	37	0.696	0.021	30	0.505	0.029	13	0.217	0.022
19.8–20.0	-4.40	44	0.657	0.016	24	0.432	0.021	17	0.139	0.014
20.0–20.2	-4.48	53	0.601	0.021	21	0.328	0.022	11	0.078	0.018
20.2–20.4	-4.56	46	0.552	0.030	37	0.225	0.018	5	0.037	0.010
20.4–20.6	-4.64	49	0.485	0.027	19	0.145	0.020	4	0.019	0.006
20.6–20.8	-4.72	53	0.426	0.028	12	0.086	0.014	0	0.007	0.005
20.8–21.0	-4.80	65	0.365	0.031	3	0.046	0.010	1	0.003	0.003
21.0–21.2	-4.88	53	0.303	0.024	4	0.020	0.006		0.001	0.001
21.2–21.4	-4.96	55	0.243	0.019	2	0.010	0.005		0.000	0.001
21.4–21.6	-5.04	48	0.165	0.020	2	0.003	0.002		0.000	0.000
21.6–21.8	-5.12	46	0.094	0.012		0.001	0.002		0.000	0.000
21.8–22.0	-5.20	25	0.052	0.014		0.000	0.001		0.000	0.000
22.0–22.2	-5.28	26	0.029	0.009		0.000	0.001		0.000	0.000
22.2–22.4	-5.36	14	0.014	0.006		0.000	0.000		0.000	0.001
22.4–22.6	-5.44	10	0.008	0.004		0.000	0.001		0.000	0.001
22.6–22.8	-5.52	7	0.004	0.003		0.000	0.000		0.000	0.001
22.8–23.0	-5.60	3	0.002	0.002		0.000	0.000		0.000	0.000
23.0–23.2	-5.68	1	0.001	0.001		0.000	0.000		0.000	0.000

* Number of source detected in each magnitude bin.

† Average of completeness estimation in 25 Monte-Carlo simulations.

‡ Standard deviation of completeness estimation for the 25 Monte-Carlo simulations.

Table 4. Detection limit (sky noise limit) and Completeness limit in μJy

filter	N3				S7				L15			
	completeness			detection	completeness			detection	completeness			detection
criterion	30%	50%	80%	5σ	30%	50%	80%	5σ	30%	50%	80%	5σ
1pt	16.3	27.7	81.9	11.2	50.8	75.5	171.4	71.3	93.6	134.2	289.6	200.9
10pt	13.1	24.0	83.0	6.0	31.7	47.5	112.5	31.5	57.0	88.1	195.2	71.2
1pt/10pt	1.24	1.15	0.99	1.87	1.60	1.59	1.52	2.27	1.64	1.52	1.48	2.82

6. discussion

6.1. improvement of sensitivity from 1pt to 10pt

Simple statistics expect a factor of $\sqrt{10/1}$ improvement in sensitivity for 10 pointed observations compared to that for a single pointed observation. However, table 4 shows that the sensitivity did not improve as well as expected.

One of the effects which degrades the sensitivity at the completeness limit is source confusion. In order to estimate the effect of source confusion, we calculate the source number density in the unit of source per beam (Table 5). In the case of the N3 band, the density is nearly equal to 1/30, the classical limit of source confusion (Condon 1974; Hogg 2001). Clearly, the observations are limited by the source confusion, and this is the reason why there is almost no improvement in the sensitivity from 1 to 10 pointed observations. In the case of the S7 and L15 bands, the density is still lower than the classical confusion limit, and there is still some room for improvement of the sensitivity by further pointed observations.

The detection limit in the L15 band shows a factor of 3 improvement which is almost as expected from simple statistics, while the detection limits in the N3 and S7 show somewhat smaller improvements than expected. The detection limit is estimated by the fluctuation of the local background where there are no sources detected. So, a smaller improvement in the detection limit means that the signal to noise ratio of the sky level is not improved by multiple observations, or alternatively that there are real fluctuations in the sky.

There are two possible causes which suppress the improvement in the S/N ratio of the sky level. (1) Incomplete sky subtraction in the co-addition stage in the pipeline creates additional noise in the final image. There are two problems which may affect the sky subtraction. The first is stray light from the Earth shine, which was not uniform over the FOV. The other is scattered light from the edge of the detector. Both create non-uniformity in the background and may prevent improvement by co-adding the frames. In order to eliminate these effects, self sky subtraction was performed, i.e. we subtracted the median value of surrounding 20×20 pixels from the value of each pixel, but there may still be some residual. The modeling of the stray light from the Earth shine is still ongoing and any data taken in the northern sky during the months of May, June and July, may suffer from the Earth shine problem, and must be handled with great care. We have modeled the scattered light from the edge of the detector, and this model will be included in the next release of the IRC imaging “pipeline”. (2) Incomplete dithering in position in multiple observations. In order to eliminate systematic errors such as flat fielding error, redundant observations, in which observations are performed by independent detector pixels, are necessary. For this purpose, dithering of the target position was performed. The AOT IRC00 which we used in this observation did not perform any dithering during each single pointed observation. Dithering of the target position must be realized among several pointed observations. Since these observa-

tions were executed in the PV phase, dithering operations among pointed observations was not implemented, at that time³. As described in section 2, only a circular change of the target position has been performed in the N3 and S7 band observations, and one directional shifting of target position has been performed in the L15 band observations. Systematic errors in the co-addition of frames may result from this incompleteness in the dithering. We have since implemented dithering among later pointed observations, and the observations taken after September 2006 do not suffer problems in dithering.

There is some possibility that we have detected real sky fluctuations. Fluctuation analysis of the background, however, is still underway, and further deeper observations (with a smaller PSF) shall be made in order to produce a clear answer to this issue. One thing we have to take care is that there may be some sources which have significant signal to noise ratio, but could not be extracted by our detection criterion (see figure 6). Comparison between the deep optical image and the AKARI S7 image shows that there are optical counterpart for some faint (below the detection limit) AKARI sources. The detection criterion which is used in this work is very simple and there is much room for improvement. Further optimization of the detection criterion may improve the detection limit.

6.2. 3 and 7 μm source counts

Figures 10 and 11 show the 3 and 7 μm number count results of the AKARI/IRC, ISO/ISOCAM and *Spitzer* IRAC surveys. The counts corrected for in-completeness are consistent with each other considering the cosmic variance.

The surveys by IRAC reached deeper than those of the IRC because of the larger aperture size of telescope and smaller size of the PSF. The IRC, however, has a larger FOV (4 times larger than that of IRAC) and a larger number of filters (6 filters from 2 to 11 μm), hence has a large merit in wide field and multi-band surveys.

6.3. 15 μm source counts

Figure 12 shows the 15 μm number count results of the AKARI/IRC, ISO/ISOCAM and *Spitzer* IRS surveys. This work is currently the widest survey below 100 μJy at this wavelength. The IRC, ISOCAM and IRS results are consistent with each other for sources brighter than 0.2 mJy, and the IRC results confirm the existence of the excess compared to the no-evolution source count models around 0.4mJy found in the ISO surveys (Elbaz et al. 1999). This excess makes itself apparent at around the 1mJy level. However, there is still a large uncer-

³ The specification of the absolute pointing accuracy of the AKARI telescope is 30 arcsec. We therefore expect that dithering in position between multiple pointed observations is achieved by scattering from positional error. Actual absolute pointing accuracy, in repeated observation for a single target position, is measured by this observation, and is turned out to be better than that of expected (the error is within FWHM of the PSF). After this observations, we implemented dithering for multi-pointed observation by shifting the target position for each pointing.

Table 5. source number density in the unit of source per beam

filter	the number of source per beam*		FWHM of PSF	
	1 pt	10pt	in pixel	in arcsec
N3	1/36.6	1/31.8	2.9	4.2
S7	1/76.7	1/56.3	2.2	5.2
L15	1/81.7	1/61.0	2.3	5.5

* The radius of the beam is set to FWHM/2.35 of the PSF.

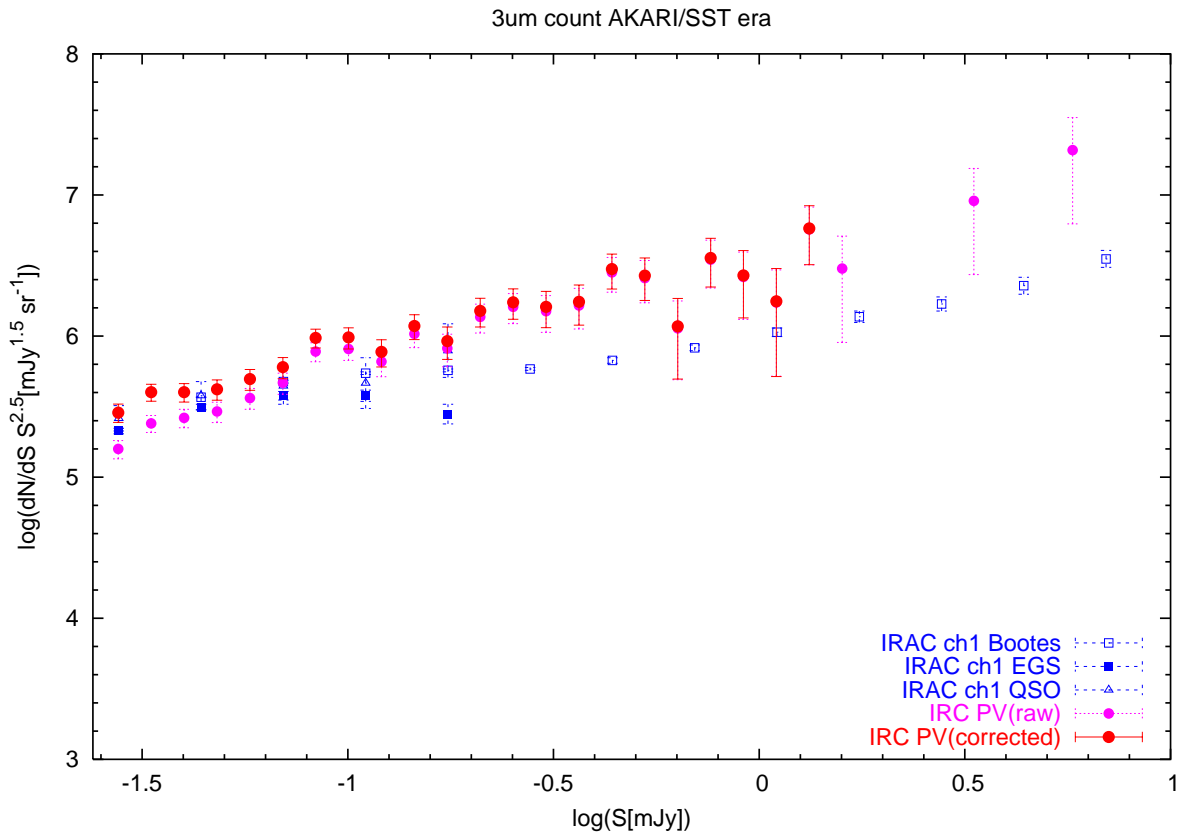


Fig. 10. AKARI/IRC 3 μm differential source counts (both raw and corrected for in-completeness) are plotted with the surveys carried out by Spitzer/IRAC results. The source counts are normalized to a Euclidian flat universe. Only flux density level above 50% completeness limit of our results is shown. IRAC channel 1 (3.6 μm) results (corrected for in-completeness) are from Fazio et al. (2004).

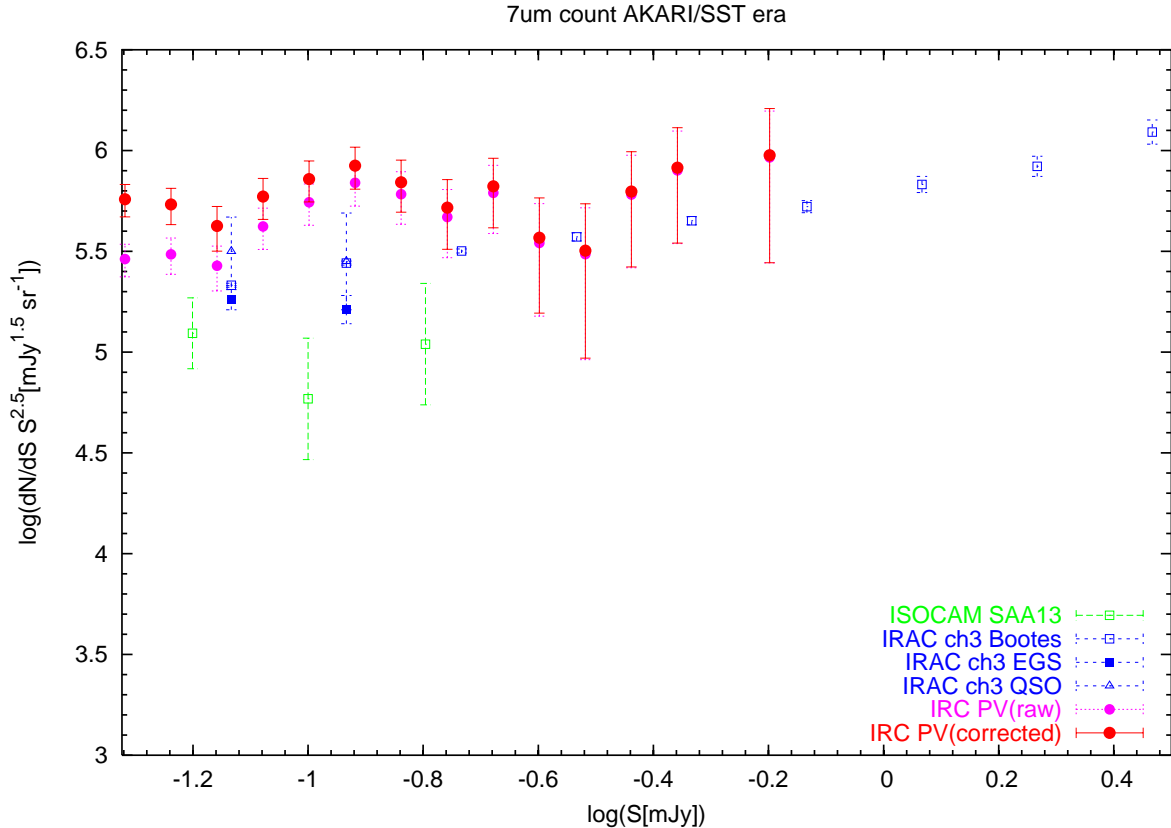


Fig. 11. AKARI/IRC 7 μm differential source counts (both raw and corrected for in-completeness) are plotted with the surveys carried out by ISO/ISOCAM and *Spitzer*/IRAC results. The source counts are normalized to a Euclidian flat universe. Only flux density level above 50% completeness limit of our results is shown. IRAC channel 3 (5.6 μm) results (corrected for in-completeness) are from Fazio et al. (2004). ISOCAM LW2 (6.7 μm) results (raw data) are from Sato et al. (2003).

tainty around the 1-10mJy flux range due to cosmological variance and calibration issues with the ISOCAM data (Vaisanen et al. 2002). The results from the deep and wide field near- and mid- infrared surveys by AKARI/IRC (the LS NEP DEEP and LS NEP WIDE surveys; Matsuhara et al. 2006) will cover this flux range and will be able to settle the issue of the normalization of the bright source counts.

The large discrepancy between the actual source counts and predictions by no-evolution models cannot be explained singly by K correction effects caused by the strong PAH emission from redshifted galaxies and some new population is required to explain the excess (e.g. Pearson 2001, Xu et al. 2003, Lagache et al. 2003, Pozzi et al. 2004, and Pearson 2005). Moreover, evolutionary models which fit both the ISO 15 μm and *Spitzer* 24 μm counts simultaneously have been already presented by Pearson (2005).

Figure 13 shows the faint end of 15 μm source counts. The raw data of the IRC results at the faint end (below 100 μJy), are consistent with the results from the *Spitzer* IRS 16 μm PUI surveys in the GOODS fields (Teplitz et al. 2005a; Teplitz et al. 2005b) in which no completeness correction is applied. The source counts corrected for incompleteness, however, agree better with the faint results from

the ISO/ISOCAM lensing survey by Altieri et al. (1999), and show a slightly higher number density than the prediction from the model fit to the the ISOCAM results (Pearson 2005). The faint end of the source counts, however, may suffer from systematic bias such as Eddington bias (Hogg & Turner 1998). An ultra deep survey by the AKARI/IRC or the *Spitzer*/IRS 16 μm PUI is essential to produce a definitive answer to the faint source counts.

7. Summary

The first near- and mid- infrared deep survey with the Infrared Camera onboard AKARI has been successfully completed in the performance verification phase of the mission. A total of 10 pointed observations have covered 86.0, 70.3, and 77.3 arcmin² area, with effective integration times of 4529, 4908, and 4417 seconds at 3, 7, and 15 μm , have detected 955, 298 and 277 sources, respectively. The 5 σ detection limits of the survey are 6.0, 31.5 and 71.2 μJy and the 50 % completeness limit are 24.0, 47.5, and 88.1 μJy at 3, 7, and 15 μm , respectively. The observation is limited by source confusion at 3 μm .

We have confirmed the turnover of the differential source counts around 400 μJy discovered by the ISO 15 μm surveys. The faint end of our 15 μm raw source counts

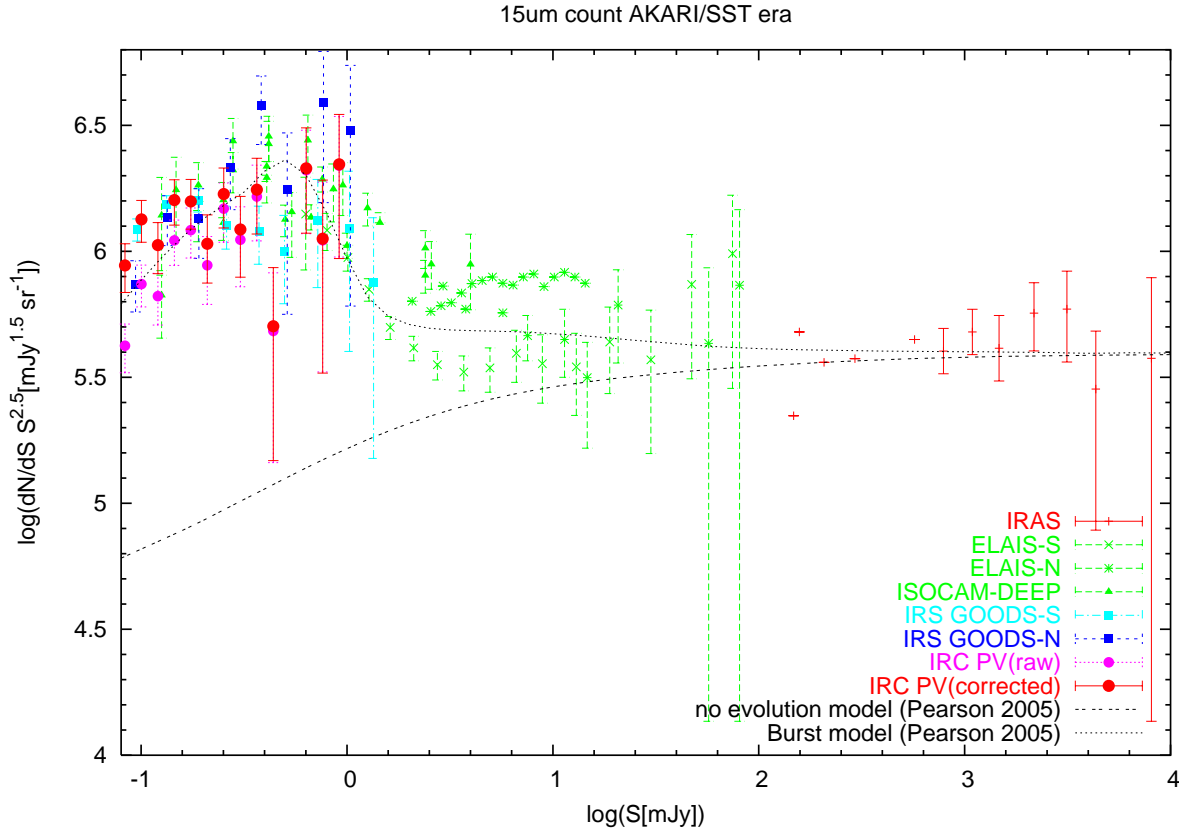


Fig. 12. AKARI/IRC 15 μm differential source counts (both raw and corrected for in-completeness) are plotted with the surveys carried out by IRAS (shifted from 12 μm), ISO/ISOCAM and Spitzer/IRS results. The source counts are normalized to a Euclidian flat universe. A no-evolution model and the contemporary evolutionary model of Pearson (2005) are also plotted for reference. Only flux density level above 50% completeness limit of our results is shown. Spitzer/IRS results are from GOODS-N (Teplitz et al. 2005a) and GOODS-S (Teplitz et al. 2005b) survey. Data points ISOCAM-DEEP include the ISO cluster lens survey (Altieri et al. 1999), and the ISO Hubble Deep Field surveys (Oliver et al. 1997; Aussel et al. 1999). ELAIS-S and ELAIS-N are from the European Large-Area ISO Survey (Gruppioni et al. 2002; Serjeant et al. 2000). IRAS counts are from Rush, Malkan & Spinoglio (1993).

are consistent with the Spitzer IRS results of Teplitz et al. (2005a) and the predictions from contemporary evolutionary models.

This work is based on the observations in the performance verification phase of the AKARI satellite, which is developed and operated by ISAS/JAXA with collaboration with ESA, Universities and companies in Japan, Korea, UK, and The Netherlands. The authors would like to thank all those who have been involved the AKARI project for many years.

References

- Altieri, B., et al. 1999, *A&A*, 343, L65
 Aussel, H., Cesarsky, C. J., Elbaz, D., & Starck, J. L. 1999, *A&A*, 342, 313
 Bertin, E. & Arnouts, S. 1996, *A&AS*, 117, 393
 Chary, R., & Elbaz, D. 2001, *ApJ*, 556, 562
 Condon, J. J. 1974, *ApJ*, 188, 279
 Elbaz, D., et al. 1999, *A&A*, 351, L37
 Fazio, G. G., et al. 2004, *ApJS*, 154, 10
 Gruppioni, C., Lari, C., Pozzi, F., Zamorani, G., Franceschini, A., Oliver, S., Rowan-Robinson, M., & Serjeant, S. 2002, *MNRAS*, 335, 831
 Hogg, D. W. 2001, *AJ*, 121, 1207
 Hogg, D. W., & Turner, E. L. 1998, *PASP*, 110, 727
 Ishihara, D., et al. 2006, *PASP*, 118, 324
 Ita, Y et al. 2007, *PASJ*, submitted
 Kasliwal, M. M., Charmandaris, V., Weedman, D., Houck, J. R., Le Floch, E., Higdon, S. J. U., Armus, L., & Teplitz, H. I. 2005, *ApJ*, 634, 1
 Lagache, G., Dole, H., Puget, J-L. 2003, *MNRAS*, 338, 555
 Lorente, R., Onaka, T., Ita, Y., Ohshima, Y., & Pearson, P. 2007, AKARI IRC Data User Manual, ver.1.1, <http://www.ir.isas.jaxa.jp/AKARI/Observation/>
 Marleau, F. R., et al. 2004, *ApJS*, 154, 66
 Matsuhara, H., et al. 2006, *PASJ*, 58, 673
 Miyazaki, S., et al. 2002, *PASJ*, 54, 833
 Murakami, H. 2007, *PASJ*, submitted
 Ohshima, Y., et al. 2007, *PASJ*, this issue
 Oliver, S. J., et al. 1997, *MNRAS*, 289, 471
 Onaka, T., et al. 2007, *PASJ*, this issue
 Papovich, C., et al. 2004, *ApJS*, 154, 70
 Pearson, C. P. 2001, *MNRAS*325, 1511
 Pearson, C. P. 2005, *MNRAS*, 358, 1417
 Pearson, C. P., et al. 2007, *PASJ*, submitted

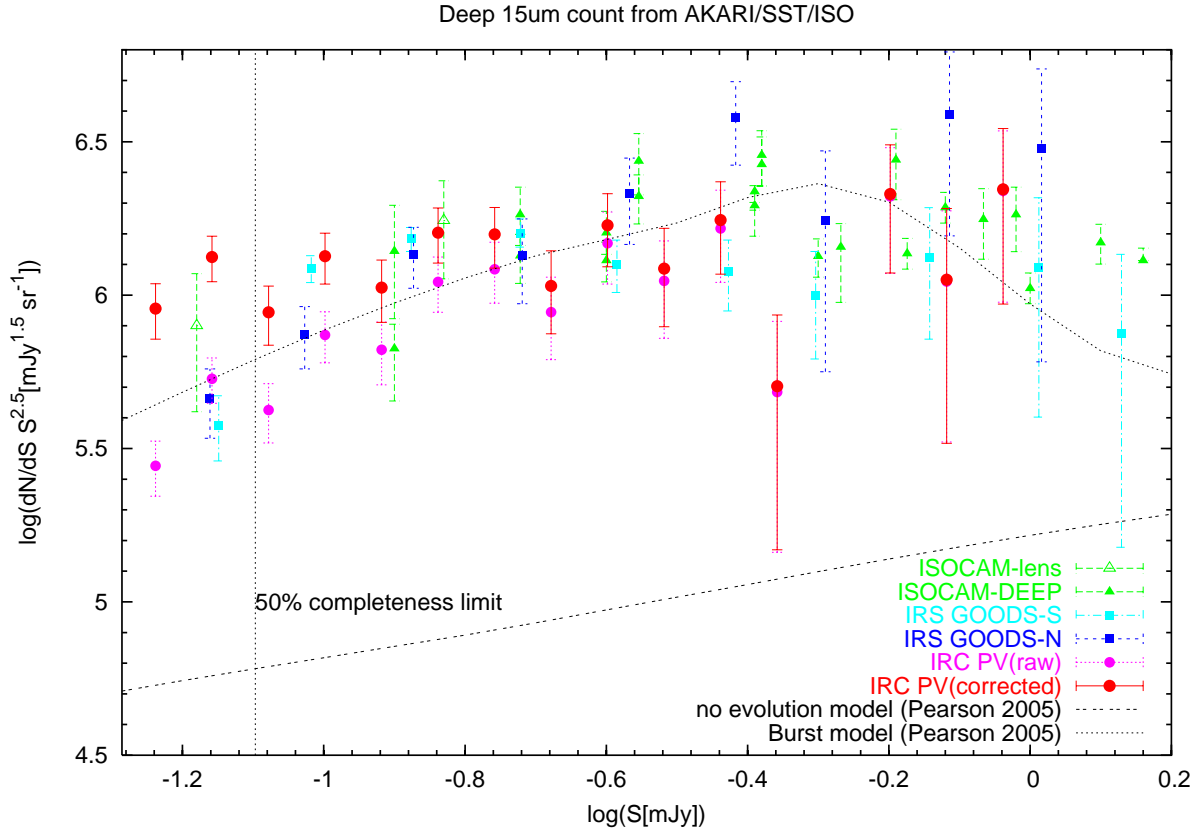


Fig. 13. The faint end of the $15 \mu\text{m}$ differential source counts. Only flux density level above 30% completeness limit of our results is shown. Correction for in-completeness may suffer from systematic bias at the fainter flux level, and 50% completeness limit of our results is shown for reference. Open triangles are data from the ISO gravitational lensing cluster survey of Altieri et al. (1999). Note that no correction for in-completeness is applied for Spitzer/IRS results.

- Pozzi, F., et al. 2004, MNRAS, 609, 122
 Rush, B., Malkan, M., & Spinoglio, L. 1993, ApJS, 89, 1
 Sato, Y, et al. 2003, A&A, 405, 833
 Serjeant, S. B. G., et al. 2000, MNRAS, 316, 768
 Takagi, T., & Pearson, C. P. 2005, MNRAS, 357, 165
 Teplitz, H. I., Charmandaris, V., Chary, R., Colbert, J.W.,
 Armus, L., & Weedman, D. 2005a, ApJ, 634, 128
 Teplitz, H. I. 2005b, presented in "When UV meets
 IR: a History of Star Formation", XXVth MORIOND
 ASTROPHYSICS MEETING, held in La Thuile, Italy,
 March 6-12, 2005
 Vaisanen, P., et al. 2002, MNRAS, MNRAS, 337, 1043
 Wada, T., et al. 2002, AdSpR, 30, 2111
 Wada, T., et al. 2007, in preparation
 Xu, C., Lonsdale, C. J., Shupe, D. L., Franceschini, A.,
 Martin, C., Schiminovich, D. 2003, ApJ, 587, 90